

## RESEARCH ARTICLE

 View Article Online  
View Journal | View Issue

 Cite this: *Inorg. Chem. Front.*, 2023, **10**, 2014

# Rare-earth La-doped VS<sub>2-x</sub> for electrochemical nitrate reduction to ammonia†

 Guohui Wang,<sup>‡a</sup> Peng Shen,<sup>‡a</sup> Kai Chen,<sup>a</sup> Yali Guo,<sup>a</sup> Xiaolin Zhao<sup>b</sup> and Ke Chu<sup>id</sup>\*<sup>a</sup>

We report rare-earth La-doped VS<sub>2-x</sub> enriched with S-vacancies (La-VS<sub>2-x</sub>) towards the electrochemical nitrate reduction to ammonia (NO<sub>3</sub>RR), which shows a maximum NH<sub>3</sub>-faradaic efficiency of 96.6% with a corresponding NH<sub>3</sub> yield rate of 11.3 mg h<sup>-1</sup> cm<sup>-2</sup> at -0.6 V vs. RHE. Theoretical computations unveil that La-dopants and S-vacancies synergistically promote NO<sub>3</sub><sup>-</sup> activation, suppress hydrogen evolution and lower the energetic barriers, leading to the enhanced NO<sub>3</sub>RR activity and selectivity of La-VS<sub>2-x</sub>.

Received 29th December 2022,

Accepted 13th February 2023

DOI: 10.1039/d2qi02757g

rsc.li/frontiers-inorganic

## 1. Introduction

NH<sub>3</sub>, a value-added chemical and also a renewable hydrogen-rich carrier, is vital to modern agriculture and industry.<sup>1-3</sup> Electrochemical nitrate reduction to ammonia (NO<sub>3</sub>RR) represents a fascinating approach to realising both green NH<sub>3</sub> generation and wastewater purification.<sup>4-6</sup> However, NO<sub>3</sub>RR effectiveness is still retarded by the complex multi-electron transfer process and easy occurrence of side reactions especially competing for the hydrogen evolution reaction (HER).<sup>7-9</sup> Therefore, it is urgently required to explore effective NO<sub>3</sub>RR electrocatalysts for active and selective NO<sub>3</sub><sup>-</sup>-to-NH<sub>3</sub> conversion.<sup>10-14</sup>

To date, substantial efforts have been devoted to exploring many potential NO<sub>3</sub>RR catalysts.<sup>15-25</sup> Metal chalcogenides have attracted wide attention in electrolysis due to their layered structure and high electrochemical stability.<sup>26-28</sup> Among them, VS<sub>2</sub> is most appealing due to its metallic nature with high conductivity, facilitating accelerated electron transfer for boosting the catalytic kinetics.<sup>29,30</sup> Nevertheless, investigations on VS<sub>2</sub>-based catalysts for the NO<sub>3</sub>RR remain largely unexplored due presumably to the poor intrinsic activity of VS<sub>2</sub> for NO<sub>3</sub><sup>-</sup> activation. Metal doping is a promis-

ing approach to tuning the surface electronic structure of the catalysts to significantly enhance the catalytic activity.<sup>31</sup> By virtue of the unique 4f structure and rich redox capability, rare-earth lanthanides emerge as intriguing metal dopants to considerably improve the catalyst activities.<sup>32-34</sup> Nevertheless, the use of rare-earth metal dopants to tune the electronic structure and NO<sub>3</sub>RR activity of the catalysts has not yet been explored.

In this study, we report a rare-earth La-doped VS<sub>2-x</sub> (La-VS<sub>2-x</sub>) enriched with S-vacancies (V<sub>S</sub>) towards the NO<sub>3</sub>RR. La-VS<sub>2-x</sub> delivers excellent NO<sub>3</sub>RR performance with a highest NH<sub>3</sub>-faradaic efficiency (FE<sub>NH<sub>3</sub></sub>) of 96.6% with the corresponding NH<sub>3</sub> yield of 11.3 mg h<sup>-1</sup> cm<sup>-2</sup> at -0.6 V vs. RHE. Detailed experiments combined with theoretical investigations are employed to unravel the catalytic NO<sub>3</sub>RR mechanism of La-VS<sub>2-x</sub>.

## 2. Results and discussion

La-VS<sub>2-x</sub> (4.8 wt% La) grown on carbon cloth (CC) was fabricated using a simple hydrothermal approach. The XRD pattern of La-VS<sub>2-x</sub> (Fig. 1a) shows major diffraction peaks assigned to the hexagonal VS<sub>2</sub> phase (JCPDS No. 89-1640). The SEM image of La-VS<sub>2-x</sub> (Fig. 1b) shows numerous nanosheets which grow perpendicularly on the CC substrate, and the nanosheet morphology of La-VS<sub>2-x</sub> is further verified by the TEM image (Fig. 1c). The elemental mapping images of La-VS<sub>2-x</sub> (Fig. 1d) reveal a uniform distribution of La elements. The HRTEM image of La-VS<sub>2-x</sub> (Fig. 1e) shows two d spacings of 0.25 and 0.60 nm, corresponding to the (011) and (001) facets of VS<sub>2</sub>, respectively. The corresponding

<sup>a</sup>School of Materials Science and Engineering, Lanzhou Jiaotong University, Lanzhou 730070, China. E-mail: chuk630@mail.lzjtu.cn

<sup>b</sup>National Engineering Laboratory for Electric Vehicles, Beijing Institute of Technology, Beijing 100081, Beijing, China

† Electronic supplementary information (ESI) available. See DOI: <https://doi.org/10.1039/d2qi02757g>

‡ These authors contributed equally to this work.

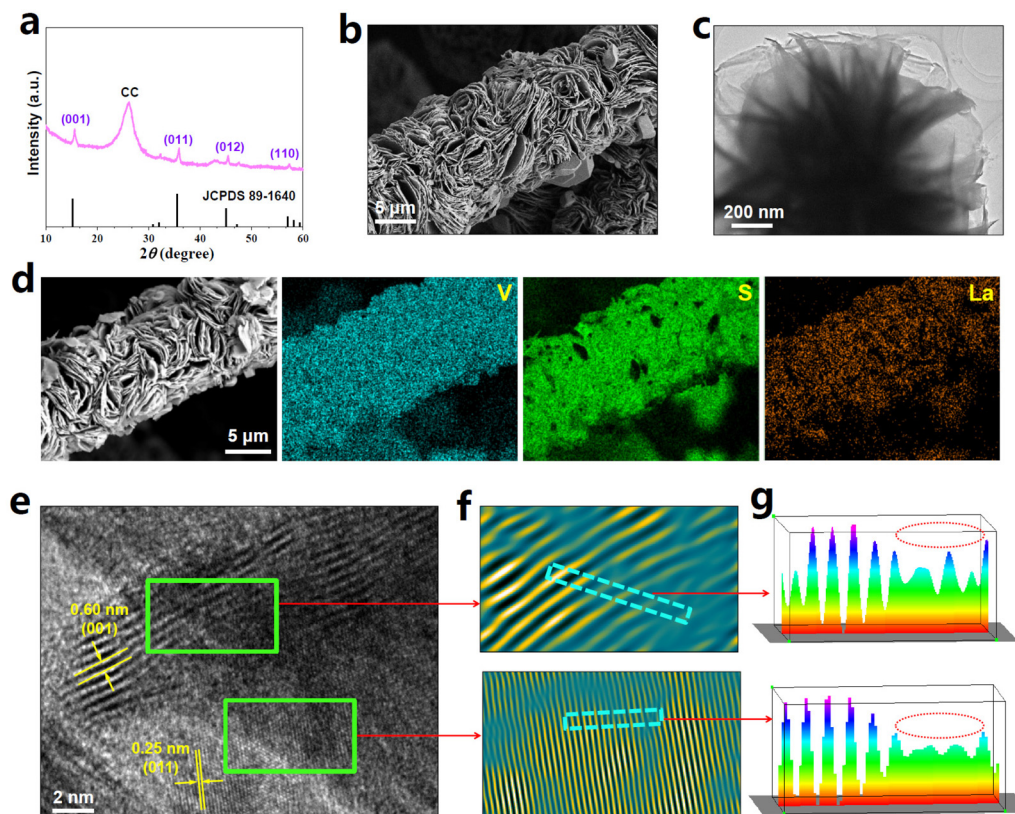


**Fig. 1** (a) XRD pattern of La- $\text{VS}_{2-x}$  on CC. (b) SEM image of La- $\text{VS}_{2-x}$  on CC. (c) TEM image of La- $\text{VS}_{2-x}$ . (d) Elemental mapping images of La- $\text{VS}_{2-x}$  on CC. (e) HRTEM image of La- $\text{VS}_{2-x}$  and (f) the corresponding IFFT pattern and (g) lattice line scanning analyses.

inverse fast Fourier transform (IFFT) pattern (Fig. 1f) and lattice line scanning analysis (Fig. 1g) signify the loss of some lattice atoms (dotted circles), indicating the presence of abundant defects/vacancies on La- $\text{VS}_{2-x}$ .<sup>35</sup> The elemental analysis further reveals a much reduced S/V molar ratio of 1.85 compared to the nominal ratio of  $\text{VS}_2$  (2), demonstrating the  $\text{V}_\text{S}$ -rich nature of La- $\text{VS}_{2-x}$ .<sup>36</sup>

As shown in the electron paramagnetic resonance (EPR) spectrum (Fig. 2a), La- $\text{VS}_{2-x}$  displays a much enhanced EPR signal compared to pristine  $\text{VS}_2$ , further attesting to the existence of abundant  $\text{V}_\text{S}$  on La- $\text{VS}_{2-x}$ .<sup>36-39</sup> The X-ray absorption near-edge structure (XANES) spectra (Fig. 2b) show that the white line intensity of La- $\text{VS}_{2-x}$  is lower than that of the  $\text{La}_2\text{O}_3$  reference, suggesting that La-dopants carry a partially positive charge.<sup>40</sup> The extended X-ray absorption fine structure (EXAFS) spectra (Fig. 2c) show that La- $\text{VS}_{2-x}$  presents a dominant peak at 2.16 Å, assigned to the La-S scattering path. Besides, no La-La (3.96 Å) scattering paths can be detected, confirming that La-dopants are atomically dispersed in La- $\text{VS}_{2-x}$ . The evidence for the presence of atomically dispersed La-dopants in La- $\text{VS}_{2-x}$  can be further proved by the wavelet transform (WT) plots (Fig. 2d), showing the absence of a La-La signal in La- $\text{VS}_{2-x}$ .<sup>41-43</sup> The EXAFS fitting results (Fig. 2e, Table S1†) reveal that the La-S coordination is around 5, implying that La-

dopants mainly substitute the five-fold coordinated V atoms of  $\text{VS}_{2-x}$  (Fig. 2f).

Theoretical calculations are carried out to examine the electronic structure of La- $\text{VS}_{2-x}$ . The calculated La-dopant formation energy ( $E_{\text{La}}$ , Fig. S1†) reveals a much reduced  $E_{\text{La}}$  of La- $\text{VS}_{2-x}$  (1.94 eV) compared to  $\text{V}_\text{S}$ -free La- $\text{VS}_2$  (3.61 eV), suggesting that  $\text{V}_\text{S}$  plays a critical role in making the incorporation of La-dopants into  $\text{VS}_{2-x}$  lattices more thermodynamically feasible.<sup>43,44</sup> Electron contour maps reveal abundant electrons accumulated in the  $\text{V}_\text{S}$  region (Fig. S2 and S3†), while La-dopant affects little the electron accumulation nature of  $\text{V}_\text{S}$  in La- $\text{VS}_{2-x}$  (Fig. 2g). These accumulated electrons are apt to be transferred to the antibonding orbital of  $\text{NO}_3^-$  for the activation and dissociation of the N=O bond,<sup>5,45</sup> facilitating the boosted  $\text{NO}_3\text{RR}$  process. The partial densities of states (PDOS) plot of La- $\text{VS}_{2-x}$  (Fig. S4†) reveals a significant La/S orbital hybridization, suggesting the strong La-S electronic interactions which allow La-dopants to be atomically dispersed and firmly stabilized in  $\text{VS}_{2-x}$ , resulting in the high thermodynamic stability of La- $\text{VS}_{2-x}$  (Fig. S5†).<sup>46</sup> Furthermore, compared to  $\text{VS}_2$  and  $\text{VS}_{2-x}$ , La-dopant incorporation makes La- $\text{VS}_{2-x}$  exhibit the occupied electron states across the Fermi level (Fig. 2h) and reduced work function (Fig. S6†), thus endowing La- $\text{VS}_{2-x}$  with enhanced conduc-

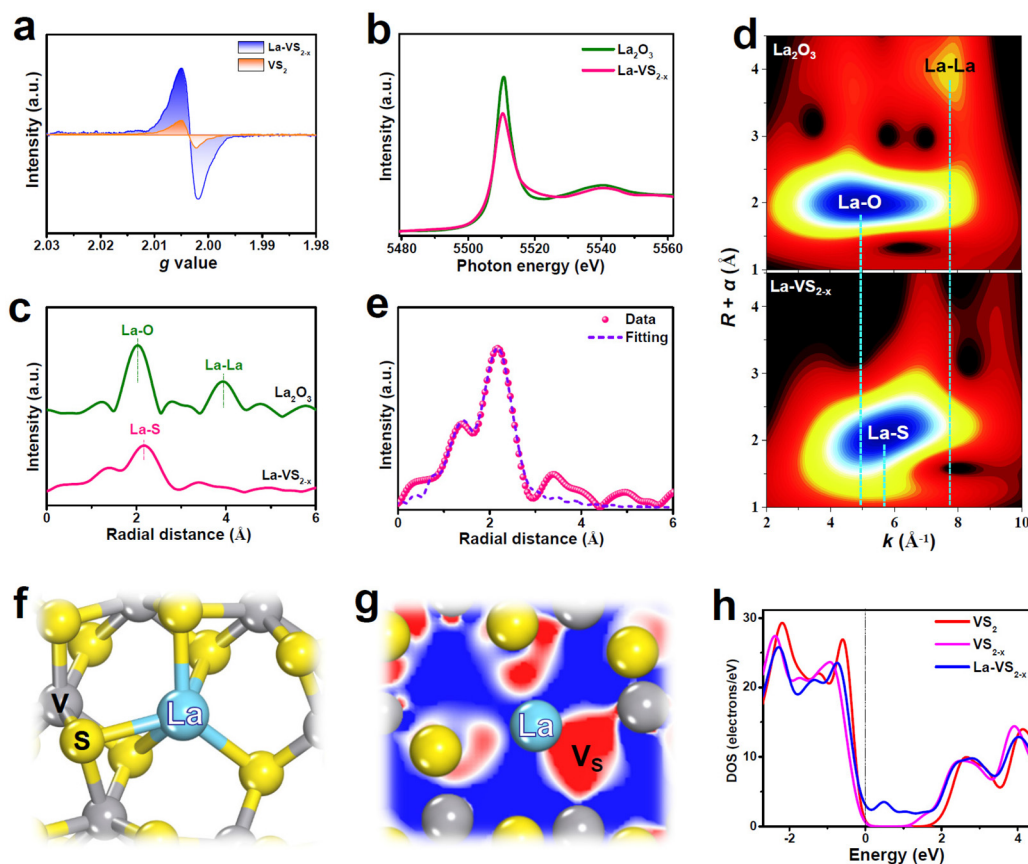


**Fig. 2** (a) EPR spectra of  $\text{VS}_2$  and  $\text{La-VS}_{2-x}$ . (b)  $\text{La L}_3$ -edge XANES, (c) EXAFS spectra and (d) WT profiles of  $\text{La-VS}_{2-x}$  and reference  $\text{La}_2\text{O}_3$ . (e) EXAFS fitting curve of  $\text{La-VS}_{2-x}$  and (f) the corresponding fitting model. (g) Electron contour map of  $\text{La-VS}_{2-x}$  (red: charge accumulation, blue: charge depletion). (h) DOS plots of  $\text{VS}_2$ ,  $\text{VS}_{2-x}$  and  $\text{La-VS}_{2-x}$ .

tivity to accelerate electron transfer and catalytic kinetics (Fig. S7†).<sup>47–51</sup>

The electrochemical  $\text{NO}_3\text{RR}$  activity of  $\text{La-VS}_{2-x}$  directly used as the working electrode is evaluated in an H-type cell on the basis of a standard procedure flow chart (Fig. S8†).<sup>52–55</sup> The electrolyte used is 0.5 M  $\text{Na}_2\text{SO}_4$  with 0.1 M  $\text{NaNO}_3$  (Fig. S9†). As displayed in Fig. 3a,  $\text{La-VS}_{2-x}$  exhibits a much higher current density in the presence of  $\text{NO}_3^-$ , indicating that  $\text{La-VS}_{2-x}$  is catalytically effective towards the  $\text{NO}_3\text{RR}$ . The  $\text{NH}_3$  yield rates and  $\text{FE}_{\text{NH}_3}$  of  $\text{La-VS}_{2-x}$  are then quantitatively estimated by the combination of chronoamperometric (Fig. S10†) and colorimetric approaches (Fig. S11–S13†).<sup>56–59</sup> As shown in Fig. 3b,  $\text{La-VS}_{2-x}$  exhibits the highest  $\text{FE}_{\text{NH}_3}$  of 96.6% at  $-0.6$  V. The corresponding  $\text{NH}_3$  yield rate and partial current density at  $-0.6$  V are  $11.3 \text{ mg h}^{-1} \text{ cm}^{-2}$  and  $121.2 \text{ mA cm}^{-2}$  (Fig. S14†), respectively. Such  $\text{NO}_3\text{RR}$  performance of  $\text{La-VS}_{2-x}$  exceeds that of most reported  $\text{NO}_3\text{RR}$  catalysts (Fig. 3c, Table S2†). We also investigate the effect of the La-dopant content on the  $\text{NO}_3\text{RR}$  performance of  $\text{La-VS}_{2-x}$  and determine that 4.8 wt% is the optimum La-dopant content (Fig. S15†). Meanwhile,  $\text{FE}_{\text{NH}_3}$  is dramatically higher than the FEs of other byproducts shown in Fig. 3d,

demonstrating the exceptional selectivity of  $\text{La-VS}_{2-x}$  for electrocatalytic  $\text{NO}_3^-$ -to- $\text{NH}_3$  conversion.

Several control tests are carried out to validate the  $\text{NH}_3$  origin. It is shown in Fig. S16† that  $\text{NH}_3$  is barely detected both in the  $\text{NO}_3^-$ -free electrolyte and at the open circuit potential (OCP). The N source is further confirmed by isotopic labeling  $^1\text{H}$  nuclear magnetic resonance (NMR) spectroscopy (Fig. 3e). Visibly, upon using  $^{14}\text{NO}_3^-$  and  $^{15}\text{NO}_3^-$  tracing agents, the resulting NMR spectra show three characteristic signals of  $^{14}\text{NH}_4^+$  and two signals of  $^{15}\text{NH}_4^+$ , respectively, proving that the detected  $\text{NH}_3$  originates from the  $\text{NO}_3\text{RR}$ .<sup>60–62</sup> We further tested the catalytic stability of  $\text{La-VS}_{2-x}$  for the  $\text{NO}_3\text{RR}$ . Fig. 3f depicts no obvious decay in  $\text{NH}_3$  yield rates and  $\text{FE}_{\text{NH}_3}$  during ten consecutive  $\text{NO}_3\text{RR}$  cycles, indicating the good cycling durability of  $\text{La-VS}_{2-x}$ . During the chronopotentiometric test for 20 h of continuous electrolysis (Fig. 3g), negligible variations in current density and corresponding  $\text{FE}_{\text{NH}_3}$  can be observed, suggesting the outstanding long-term stability of  $\text{La-VS}_{2-x}$ . After the stability tests,  $\text{La-VS}_{2-x}$  reveals no obvious changes in the morphology, crystal phase and La content (Fig. S17†), confirming the robust structural and compositional stability of  $\text{La-VS}_{2-x}$ .



**Fig. 3** (a) LSV curves of La- $\text{VS}_{2-x}$  with and without the addition of 0.1 M  $\text{NO}_3^-$ . (b)  $\text{NH}_3$  yield rates and  $\text{FE}_{\text{NH}_3}$  of La- $\text{VS}_{2-x}$  at various potentials. (c)  $\text{NO}_3\text{RR}$  performance comparison between La- $\text{VS}_{2-x}$  and reported catalysts. (d) FEs of different products after  $\text{NO}_3\text{RR}$  electrolysis at various potentials. (e)  $^1\text{H}$  NMR measurements fed by  $^{14}\text{NO}_3^-/^{15}\text{NO}_3^-$  after  $\text{NO}_3\text{RR}$  electrolysis. (f) Cycling and (g) long-term chronoamperometry tests at  $-0.6$  V. (h) Comparison of the  $\text{NO}_3\text{RR}$  performance between  $\text{VS}_2$  and La- $\text{VS}_{2-x}$  at  $-0.6$  V.

We also evaluate the  $\text{NO}_3\text{RR}$  activity of pristine  $\text{VS}_2$  under the same conditions at  $-0.6$  V (Fig. 3h). Obviously, the  $\text{NO}_3\text{RR}$  performance of  $\text{VS}_{2-x}$  is considerably lower than that of La- $\text{VS}_{2-x}$ , with  $\text{FE}_{\text{NH}_3}$  and the corresponding  $\text{NH}_3$  yield rate being 1.4 and 1.9 times poorer than those of La- $\text{VS}_{2-x}$ , respectively, suggesting that La-dopants have a significant contribution to the  $\text{NO}_3\text{RR}$  activity of La- $\text{VS}_{2-x}$ . We measured the electrochemical surface areas (ECSAs) of the two catalysts and found that the ECSA-normalized performance of La- $\text{VS}_{2-x}$  is still considerably better than that of  $\text{VS}_2$  (Fig. S18<sup>†</sup>), indicating the superior intrinsic  $\text{NO}_3\text{RR}$  activity of La- $\text{VS}_{2-x}$ . The in-depth mechanistic understanding of the enhanced  $\text{NO}_3\text{RR}$  of La- $\text{VS}_{2-x}$  is elucidated by theoretical investigations.

Since  $\text{NO}_3^-$  adsorption is a critical prerequisite for the  $\text{NO}_3\text{RR}$ ,<sup>63</sup> we first examined  $\text{NO}_3^-$  adsorption on various catalysts. As shown in Fig. S19,<sup>†</sup> in contrast to the negligible N=O bond elongation on pristine  $\text{VS}_2$ , the N=O bond of the adsorbed  $\text{NO}_3^-$  on the  $\text{V}_s$  site of  $\text{VS}_{2-x}$  is stretched to 1.305 Å, and it is further stretched to 1.365 Å on La-dopant-adjacent  $\text{V}_s$  site of La- $\text{VS}_{2-x}$ , indicating that  $\text{NO}_3^-$  can be significantly activated on La- $\text{VS}_{2-x}$ . This is further corroborated by the differential charge density maps, showing that compared to the cases of  $\text{VS}_2$  and  $\text{VS}_{2-x}$  (Fig. S20<sup>†</sup>), La- $\text{VS}_{2-x}$  exhibits a more intense charge transfer with the adsorbed  $\text{NO}_3^-$  (Fig. 4a). The corresponding electron location function maps (Fig. 4b) reveal that

both the  $\text{V}_s$ -induced unsaturated V atom and the La-dopant (or La- $\text{V}_s$  site) synergistically donate electrons to the adsorbed  $\text{NO}_3^-$ ,<sup>35</sup> resulting in effective  $\text{NO}_3^-$  activation on La- $\text{VS}_{2-x}$ . Benefitting from the enhanced  $\text{NO}_3^-$  activation on the La- $\text{V}_s$  site, La- $\text{VS}_{2-x}$  shows a largely reduced binding free energy of  $\text{NO}_3^-$  relative to  $\text{VS}_2$  and  $\text{VS}_{2-x}$  (Fig. 4c), thus facilitating the subsequent  $\text{NO}_3\text{RR}$  process. Meanwhile, compared to the  $\text{V}_s$  site of  $\text{VS}_{2-x}$ , the La- $\text{V}_s$  site of La- $\text{VS}_{2-x}$  exhibits a more energy requirement for  $\text{H}_2$  evolution (Fig. 4d), and thus La- $\text{VS}_{2-x}$  can effectively impede the HER to benefit  $\text{NO}_3\text{RR}$  selectivity.<sup>56</sup>

The free energy changes of  $\text{NO}_3\text{RR}$  pathways of all considered  $\text{VS}_2$ ,  $\text{VS}_{2-x}$  and La- $\text{VS}_{2-x}$  catalysts are further assessed, with their corresponding atom configurations being displayed in Fig. S21–S23.<sup>†</sup> It is known that the electrocatalytic  $\text{NO}_3\text{RR}$  process for  $\text{NH}_3$  formation comprises the initial deoxidation steps of  $^*\text{NO}_3 \rightarrow ^*\text{NO}_2 \rightarrow ^*\text{NO}$  and the following hydrogenation steps of  $^*\text{NOH} \rightarrow ^*\text{N} \rightarrow ^*\text{NH} \rightarrow ^*\text{NH}_2 \rightarrow ^*\text{NH}_3$ .<sup>64–66</sup> As shown in Fig. 4e, in comparison with  $\text{VS}_2$  and  $\text{VS}_{2-x}$ , La- $\text{VS}_{2-x}$  shows the lowest energy barrier of  $-0.63$  eV for its rate-determining step (RDS) of  $^*\text{NO} \rightarrow ^*\text{NOH}$ , suggesting its favorable energetics to boost the  $\text{NO}_3\text{RR}$  process. Therefore, the co-introduction of  $\text{V}_s$  and La-dopants can synergistically promote  $\text{NO}_3^-$  activation, retard the HER and lower the reaction energetic barriers, thereby greatly promoting the  $\text{NO}_3\text{RR}$  activity and selectivity of La- $\text{VS}_{2-x}$  for  $\text{NO}_3^-$ -to- $\text{NH}_3$  conversion.



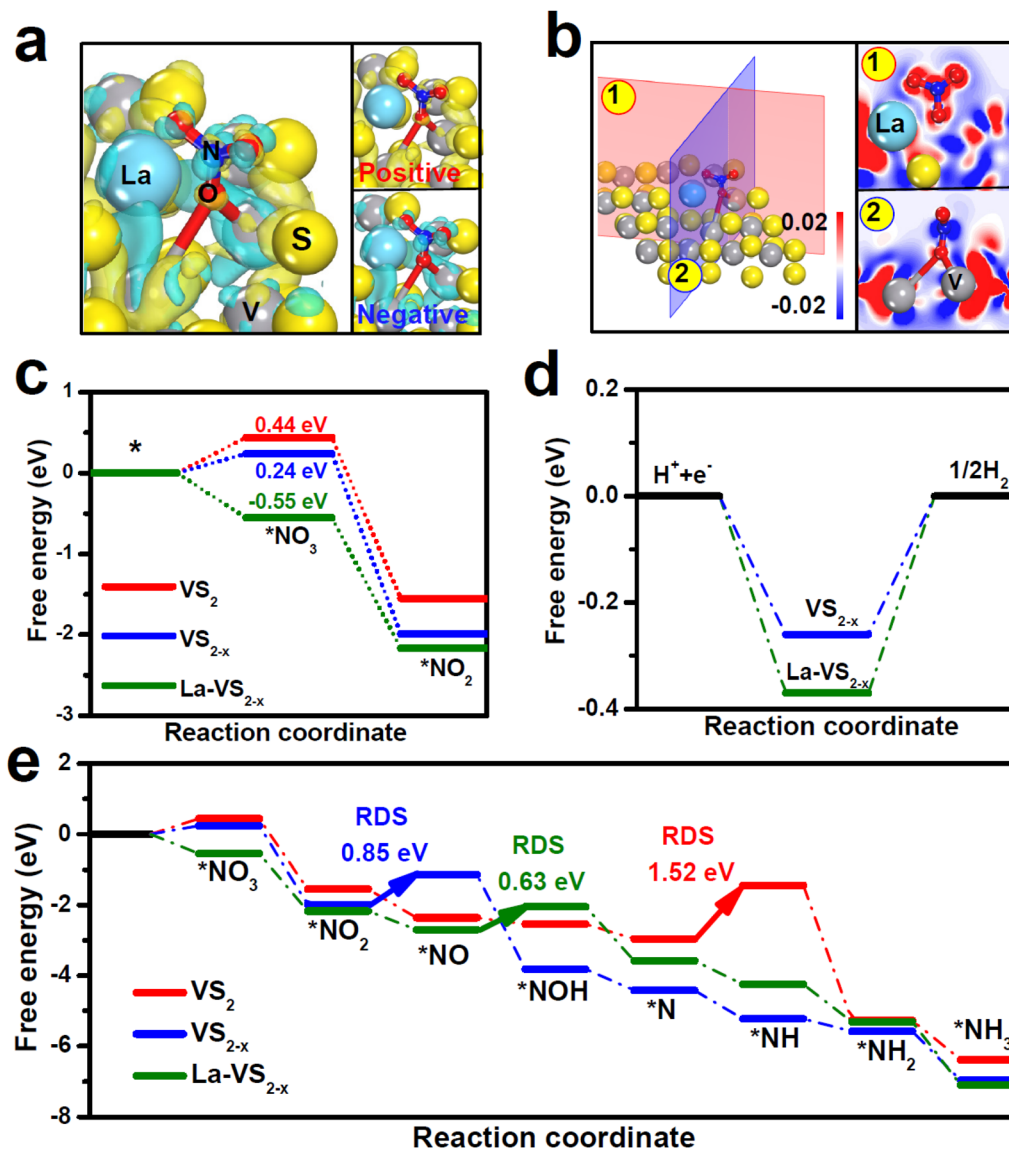


Fig. 4 (a) Differential charge density maps of  $\text{NO}_3^-$  adsorption on  $\text{La-VS}_{2-x}$  (yellow: accumulation, cyan: depletion) and (b) the corresponding electron location function maps (red: accumulation, blue: depletion). (c and d) Binding free energies of (c)  $\text{NO}_3^-$  and (d) H on different catalysts. (e) Gibbs free energy diagrams of the  $\text{NO}_3\text{RR}$  pathway of  $\text{VS}_2$ ,  $\text{VS}_{2-x}$  and  $\text{La-VS}_{2-x}$ , respectively.

### 3. Conclusion

In summary,  $\text{La-VS}_{2-x}$  is verified to be a highly active and selective  $\text{NO}_3\text{RR}$  catalyst. Theoretical computations reveal that the excellent  $\text{NO}_3\text{RR}$  performance of  $\text{La-VS}_{2-x}$  originates from the synergy of La-dopants and  $\text{V}_s$  to promote  $\text{NO}_3^-$  activation, suppress the HER and lower the energetic barriers. This work demonstrates the great potential of rare earth catalysts toward the efficient  $\text{NO}_3\text{RR}$  for  $\text{NH}_3$  electro-synthesis.

### Conflicts of interest

There are no conflicts of interest to declare.

### Acknowledgements

This work was supported by the Central Government Guides Local Science and Technology Development Project (206Z1003G) and the Longyuan Youth Innovative and Entrepreneurial Talents Project ([2021]17).

### References

- 1 J. Liang, Q. Liu, A. A. Alshehri and X. Sun, Recent advances in nanostructured heterogeneous catalysts for N-cycle electrocatalysis, *Nano Res. Energy*, 2022, **1**, e9120010.

- 2 K. Chen, P. Shen, N. Zhang, D. Ma and K. Chu, Electrocatalytic NO reduction to  $\text{NH}_3$  on  $\text{Mo}_2\text{C}$  nanosheets, *Inorg. Chem.*, 2023, **62**, 653–658.
- 3 D. Qi, F. Lv, T. Wei, M. Jin, G. Meng, S. Zhang, Q. Liu, W. Liu, D. Ma, M. S. Hamdy, J. Luo and X. Liu, High-efficiency electrocatalytic NO reduction to  $\text{NH}_3$  by nanoporous VN, *Nano Res. Energy*, 2022, **1**, e9120022.
- 4 H. Xu, Y. Ma, J. Chen, W.-x. Zhang and J. Yang, Electrocatalytic reduction of nitrate—a step towards a sustainable nitrogen cycle, *Chem. Soc. Rev.*, 2022, **51**, 2710–2758.
- 5 Y. Wang, C. Wang, M. Li, Y. Yu and B. Zhang, Nitrate electroreduction: mechanism insight, in situ characterization, performance evaluation, and challenges, *Chem. Soc. Rev.*, 2021, **50**, 6720–6733.
- 6 P. H. van Langevelde, I. Katsounaros and M. T. Koper, Electrocatalytic nitrate reduction for sustainable ammonia production, *Joule*, 2021, **5**, 290–294.
- 7 N. Zhang, J. Shang, X. Deng, L. Cai, R. Long, Y. Xiong and Y. Chai, Governing interlayer strain in bismuth nanocrystals for efficient ammonia electrosynthesis from nitrate reduction, *ACS Nano*, 2022, **16**, 4795–4804.
- 8 Y. Wang, H. Li, W. Zhou, X. Zhang, B. Zhang and Y. Yu, Structurally disordered  $\text{RuO}_2$  nanosheets with rich oxygen vacancies for enhanced nitrate electroreduction to ammonia, *Angew. Chem.*, 2022, **134**, e202202604.
- 9 H. Liu, X. Lang, C. Zhu, J. Timoshenko, M. Rüscher, L. Bai, N. Guijarro, H. Yin, Y. Peng, J. Li, W. Wang, B. Roldan Cuenya and J. Luo, Efficient electrochemical nitrate reduction to ammonia with copper-supported rhodium cluster and single-atom catalysts, *Angew. Chem.*, 2022, **134**, e202202556.
- 10 Q. Gao, H. S. Pillai, Y. Huang, S. Liu, Q. Mu, X. Han, Z. Yan, H. Zhou, Q. He, H. Xin and H. Zhu, Breaking adsorption-energy scaling limitations of electrocatalytic nitrate reduction on intermetallic CuPd nanocubes by machine-learned insights, *Nat. Commun.*, 2022, **13**, 2338.
- 11 X. F. Cheng, J. H. He, H. Q. Ji, H. Y. Zhang, Q. Cao, W. J. Sun, C. L. Yan and J. M. Lu, Coordination symmetry breaking of single-atom catalysts for robust and efficient nitrate electroreduction to ammonia, *Adv. Mater.*, 2022, **34**, 2205767.
- 12 F.-Y. Chen, Z.-Y. Wu, S. Gupta, D. J. Rivera, S. V. Lambeets, S. Pecaut, J. Y. T. Kim, P. Zhu, Y. Z. Finprock, D. M. Meira, G. King, G. Gao, W. Xu, D. A. Cullen, H. Zhou, Y. Han, D. E. Perea, C. L. Muhich and H. Wang, Efficient conversion of low-concentration nitrate sources into ammonia on a Ru-dispersed Cu nanowire electrocatalyst, *Nat. Nanotechnol.*, 2022, **17**, 759–767.
- 13 Z. Deng, C. Ma, Z. Li, Y. Luo, L. Zhang, S. Sun, Q. Liu, J. Du, Q. Lu, B. Zheng and X. Sun, High-efficiency electrochemical nitrate reduction to ammonia on a  $\text{Co}_3\text{O}_4$  nanoarray catalyst with cobalt vacancies, *ACS Appl. Mater. Interfaces*, 2022, **14**, 46595–46602.
- 14 Z. Deng, C. Ma, X. Fan, Z. Li, Y. Luo, S. Sun, D. Zheng, Q. Liu, J. Du, Q. Lu, B. Zheng and X. Sun, Construction of  $\text{CoP}/\text{TiO}_2$  nanoarray for enhanced electrochemical nitrate reduction to ammonia, *Mater. Today Phys.*, 2022, **28**, 100854.
- 15 Y. Xu, Y. Wen, T. Ren, H. Yu, K. Deng, Z. Wang, X. Li, L. Wang and H. Wang, Engineering the surface chemical microenvironment over CuO nanowire arrays by polyaniline modification for efficient ammonia electrosynthesis from nitrate, *Appl. Catal., B*, 2023, **320**, 121981.
- 16 Y. Xu, Y. Sheng, M. Wang, T. Ren, K. Shi, Z. Wang, X. Li, L. Wang and H. Wang, Interface coupling induced built-in electric fields boost electrochemical nitrate reduction to ammonia over  $\text{CuO}/\text{MnO}_2$  core-shell hierarchical nanoarrays, *J. Mater. Chem. A*, 2022, **10**, 16883–16890.
- 17 T. Ren, Z. Yu, H. Yu, K. Deng, Z. Wang, X. Li, H. Wang, L. Wang and Y. Xu, Interfacial polarization in metal-organic framework reconstructed Cu/Pd/ $\text{CuO}_x$  multi-phase heterostructures for electrocatalytic nitrate reduction to ammonia, *Appl. Catal., B*, 2022, **318**, 121805.
- 18 Y. Zhang, X. Chen, W. Wang, L. Yin and J. C. Crittenden, Electrocatalytic nitrate reduction to ammonia on defective  $\text{Au}_1\text{Cu}$  (111) single-atom alloys, *Appl. Catal., B*, 2022, **310**, 121346.
- 19 X. Li, S. Wang, G. Wang, P. Shen, D. Ma and K. Chu,  $\text{Mo}_2\text{C}$  for electrocatalytic nitrate reduction to ammonia, *Dalton Trans.*, 2022, **51**, 17547–17552.
- 20 S. Zhang, M. Li, J. Li, Q. Song and X. Liu, High-ammonia selective metal-organic framework-derived Co-doped  $\text{Fe}/\text{Fe}_2\text{O}_3$  catalysts for electrochemical nitrate reduction, *Proc. Natl. Acad. Sci.*, 2022, **119**, e2115504119.
- 21 W. J. Sun, H. Q. Ji, L. X. Li, H. Y. Zhang, Z. K. Wang, J. H. He and J. M. Lu, Built-in electric field triggered interfacial accumulation effect for efficient nitrate removal at ultra-low concentration and electroreduction to ammonia, *Angew. Chem., Int. Ed.*, 2021, **60**, 22933–22939.
- 22 L. Li, C. Tang, X. Cui, Y. Zheng, X. Wang, H. Xu, S. Zhang, T. Shao, K. Davey and S. Z. Qiao, Efficient nitrogen fixation to ammonia through integration of plasma oxidation with electrocatalytic reduction, *Angew. Chem.*, 2021, **133**, 14250–14256.
- 23 P. Gao, Z. H. Xue, S. N. Zhang, D. Xu, G. Y. Zhai, Q. Y. Li, J. S. Chen and X. H. Li, Schottky barrier-induced surface electric field boosts universal reduction of  $\text{NO}_x^-$  in water to ammonia, *Angew. Chem.*, 2021, **133**, 20879–20884.
- 24 P. Li, Z. Jin, Z. Fang and G. Yu, A single-site iron catalyst with preoccupied active centers that achieves selective ammonia electrosynthesis from nitrate, *Energy Environ. Sci.*, 2021, **14**, 3522–3531.
- 25 Y. Guo, R. Zhang, S. Zhang, Y. Zhao, Q. Yang, Z. Huang, B. Dong and C. Zhi, Pd doping-weakened intermediate adsorption to promote electrocatalytic nitrate reduction on  $\text{TiO}_2$  nanoarrays for ammonia production and energy supply with zinc-nitrate batteries, *Energy Environ. Sci.*, 2021, **14**, 3938–3944.
- 26 J. Zhang, T. Wang, D. Pohl, B. Rellinghaus, R. Dong, S. Liu, X. Zhuang and X. Feng, Interface engineering of  $\text{MoS}_2/\text{Ni}_3\text{S}_2$  heterostructures for highly enhanced electrochemical

- overall-water-splitting activity, *Angew. Chem., Int. Ed.*, 2016, **55**, 6702–6707.
- 27 H. Li, C. Tsai, A. L. Koh, L. Cai, A. W. Contryman, A. H. Fragapane, J. Zhao, H. S. Han, H. C. Manoharan, F. Abild-Pedersen, J. K. Nørskov and X. Zheng, Activating and optimizing MoS<sub>2</sub> basal planes for hydrogen evolution through the formation of strained sulphur vacancies, *Nat. Mater.*, 2016, **15**, 48–53.
- 28 Q. Xiang, J. Yu and M. Jaroniec, Synergetic effect of MoS<sub>2</sub> and graphene as cocatalysts for enhanced photocatalytic H<sub>2</sub> production activity of TiO<sub>2</sub> nanoparticles, *J. Am. Chem. Soc.*, 2012, **134**, 6575–6578.
- 29 Q. Li, Y. Guo, Y. Tian, W. Liu and K. Chu, Activating VS<sub>2</sub> basal planes for enhanced NRR electrocatalysis: the synergistic role of S-vacancies and B dopants, *J. Mater. Chem. A*, 2020, **8**, 16195–16202.
- 30 J. Zhang, C. Zhang, Z. Wang, J. Zhu, Z. Wen, X. Zhao, X. Zhang, J. Xu and Z. Lu, Synergistic interlayer and defect engineering in VS<sub>2</sub> nanosheets toward efficient electrocatalytic hydrogen evolution reaction, *Small*, 2018, **14**, 1703098.
- 31 K. Chu, Y. Liu, Y. Li, Y. Guo, Y. Tian and H. Zhang, Multi-functional Mo-doping in MnO<sub>2</sub> nanoflowers toward efficient and robust electrocatalytic nitrogen fixation, *Appl. Catal., B*, 2020, **264**, 118525.
- 32 N. Liu, D. Cao, W. Liu, H. Zhang, Y. Zhu, L. Chang, D. Wu and D. Cheng, Constructing La-doped ultrathin Co-based nanostructured electrocatalysts for high-performance water oxidation process, *Int. J. Hydrogen Energy*, 2022, **47**, 14504–14514.
- 33 X. Yang, Y. Ma, Y. Liu, K. Wang, Y. Wang, M. Liu, X. Qiu, W. Li and J. Li, Defect-induced Ce-doped Bi<sub>2</sub>WO<sub>6</sub> for efficient electrocatalytic N<sub>2</sub> reduction, *ACS Appl. Mater. Interfaces*, 2021, **13**, 19864–19872.
- 34 Y. Luo, K. Chen, G. Wang, G. Zhang, N. Zhang and K. Chu, Ce-doped MoS<sub>2-x</sub> nanoflower arrays for electrocatalytic nitrate reduction to ammonia, *Inorg. Chem. Front.*, 2023, DOI: [10.1039/d2qi01798a](https://doi.org/10.1039/d2qi01798a).
- 35 P. Shen, G. Wang, K. Chen, J. Kang, D. Ma and K. Chu, Selenium-vacancy-rich WSe<sub>2</sub> for nitrate electroreduction to ammonia, *J. Colloid Interface Sci.*, 2023, **629**, 563–570.
- 36 P. Shen, X. Li, Y. Luo, Y. Guo, X. Zhao and K. Chu, High-efficiency N<sub>2</sub> electroreduction enabled by Se-vacancy-rich WSe<sub>2-x</sub> in water-in-salt electrolytes, *ACS Nano*, 2022, **16**, 7915–7925.
- 37 X. Li, G. Zhang, P. Shen, X. Zhao and K. Chu, A defect engineered p-block SnS<sub>2-x</sub> catalyst for efficient electrocatalytic NO reduction to NH<sub>3</sub>, *Inorg. Chem. Front.*, 2023, **10**, 280–287.
- 38 Y. Luo, P. Shen, X. Li, Y. Guo and K. Chu, Sulfur-deficient Bi<sub>2</sub>S<sub>3-x</sub> synergistically coupling Ti<sub>3</sub>C<sub>2</sub>T<sub>x</sub>-MXene for boosting electrocatalytic N<sub>2</sub> reduction, *Nano Res.*, 2022, **15**, 3991–3999.
- 39 Y. Luo, Q. Li, Y. Tian, Y. Liu and K. Chu, Amorphization engineered VSe<sub>2-x</sub> nanosheets with abundant Se-vacancies for enhanced N<sub>2</sub> electroreduction, *J. Mater. Chem. A*, 2022, **10**, 1742–1749.
- 40 L. Zhang, M. Zhou, A. Wang and T. Zhang, Selective hydrogenation over supported metal catalysts: from nanoparticles to single atoms, *Chem. Rev.*, 2019, **120**, 683–733.
- 41 K. Chen, Y. Zhang, J. Xiang, X. Zhao, X. Li and K. Chu, p-block antimony single-atom catalysts for nitric oxide electroreduction to ammonia, *ACS Energy Lett.*, 2023, **8**, 1281–1288.
- 42 K. Chen, G. Zhang, X. Li, X. Zhao and K. Chu, Electrochemical NO reduction to NH<sub>3</sub> on Cu single atom catalyst, *Nano Res.*, 2023, DOI: [10.1007/s12274-023-5384-9](https://doi.org/10.1007/s12274-023-5384-9).
- 43 K. Chen, J. Wang, J. Kang, X. Lu, X. Zhao and K. Chu, Atomically Fe-doped MoS<sub>2-x</sub> with Fe-Mo dual sites for efficient electrocatalytic NO reduction to NH<sub>3</sub>, *Appl. Catal., B*, 2023, **324**, 122241.
- 44 K. Chu, J. Wang, Y. Liu, Q. Li and Y. Guo, Mo-doped SnS<sub>2</sub> with rich S-vacancies for highly efficient electrocatalytic N<sub>2</sub> reduction: the critical role of Mo-Sn-Sn trimer, *J. Mater. Chem. A*, 2020, **8**, 7117–7124.
- 45 X. Li, K. Chen, X. Lu, D. Ma and K. Chu, Atomically dispersed Co catalyst for electrocatalytic NO reduction to NH<sub>3</sub>, *Chem. Eng. J.*, 2023, **454**, 140333.
- 46 X. Li, P. Shen, Y. Luo, Y. Li, Y. Guo, H. Zhang and K. Chu, PdFe single-atom alloy metallene for N<sub>2</sub> electroreduction, *Angew. Chem.*, 2022, **134**, e202205923.
- 47 P. Shen, X. Li, Y. Luo, N. Zhang, X. Zhao and K. Chu, Ultra-efficient N<sub>2</sub> electroreduction achieved over a rhodium single-atom catalyst (Rh<sub>1</sub>/MnO<sub>2</sub>) in water-in-salt electrolyte, *Appl. Catal., B*, 2022, **316**, 121651.
- 48 K. Chen, J. Wang, H. Zhang, D. Ma and K. Chu, Self-tandem electrocatalytic NO reduction to NH<sub>3</sub> on W single atom catalyst, *Nano. Lett.*, 2023, DOI: [10.1021/acs.nanolett.2c04444](https://doi.org/10.1021/acs.nanolett.2c04444).
- 49 W. Zhang, M. Jiang, S. Yang, Y. Hu, B. Mu, Z. Tie and Z. Jin, *In situ* grown CuO<sub>x</sub> nanowire forest on copper foam: A 3D hierarchical and freestanding electrocatalyst with enhanced carbonaceous product selectivity in CO<sub>2</sub> reduction, *Nano Res. Energy*, 2022, **1**, e9120033.
- 50 L. Zhang, J. Liang, L. Yue, K. Dong, J. Li, D. Zhao, Z. Li, S. Sun, Y. Luo, Q. Liu, G. Cui, A. Ali Alshehri, X. Guo and X. Sun, Benzoate anions-intercalated NiFe-layered double hydroxide nanosheet array with enhanced stability for electrochemical seawater oxidation, *Nano Res. Energy*, 2022, **1**, e9120028.
- 51 F. Guo, M. Zhang, S. Yi, X. Li, R. Xin, M. Yang, B. Liu, H. Chen, H. Li and Y. Liu, Metal-coordinated porous polydopamine nanospheres derived Fe<sub>3</sub>N-FeCo encapsulated N-doped carbon as a highly efficient electrocatalyst for oxygen reduction reaction, *Nano Res. Energy*, 2022, **1**, e9120027.
- 52 X. Li, P. Shen, X. Li, D. Ma and K. Chu, Sub-nm RuO<sub>x</sub> clusters on Pd metallene for synergistically enhanced nitrate electroreduction to ammonia, *ACS Nano*, 2023, **17**, 1081–1090.

- 53 K. Chen, Z. Ma, X. Li, J. Kang, D. Ma and K. Chu, Single-atom Bi alloyed Pd metallene for nitrate electroreduction to ammonia, *Adv. Funct. Mater.*, 2023, DOI: [10.1002/adfm.202209890](https://doi.org/10.1002/adfm.202209890).
- 54 G. Wang, P. Shen, Y. Luo, X. Li, X. Li and K. Chu, A vacancy engineered  $\text{MnO}_{2-x}$  electrocatalyst promotes electroreduction of nitrate to ammonia, *Dalton Trans.*, 2022, **51**, 9206–9212.
- 55 G. Zhang, X. Li, K. Chen, Y. Guo, D. Ma and K. Chu, Tandem electrocatalytic nitrate reduction to ammonia on MBenes, *Angew. Chem., Int. Ed.*, 2023, DOI: [10.1002/anie.202300054](https://doi.org/10.1002/anie.202300054).
- 56 N. Zhang, G. Zhang, P. Shen, H. Zhang, D. Ma and K. Chu, Lewis acid Fe-V pairs promote nitrate electroreduction to ammonia, *Adv. Funct. Mater.*, 2023, DOI: [10.1002/adfm.202211537](https://doi.org/10.1002/adfm.202211537).
- 57 Y. Luo, K. Chen, P. Shen, X. Li, X. Li, Y. Li and K. Chu, B-doped  $\text{MoS}_2$  for nitrate electroreduction to ammonia, *J. Colloid Interface Sci.*, 2023, **629**, 950–957.
- 58 K. Chu, X. Li, Q. Li, Y. Guo and H. Zhang, Synergistic enhancement of electrocatalytic nitrogen reduction over boron nitride quantum dots decorated  $\text{Nb}_2\text{CT}_x$ -MXene, *Small*, 2021, **17**, 2102363.
- 59 Y. Cheng, X. Li, P. Shen, Y. Guo and K. Chu, MXene quantum dots/copper heterostructure for synergistically enhanced  $\text{N}_2$  electroreduction, *Energy Environ. Mater.*, 2023, **6**, e12268.
- 60 Q. Li, P. Shen, Y. Tian, X. Li and K. Chu, Metal-free BN quantum dots/graphitic  $\text{C}_3\text{N}_4$  heterostructure for nitrogen reduction reaction, *J. Colloid Interface Sci.*, 2022, **606**, 204–212.
- 61 K. Chu, Y. Luo, P. Shen, X. Li, Q. Li and Y. Guo, Unveiling the synergy of O-vacancy and heterostructure over  $\text{MoO}_{3-x}$ /MXene for  $\text{N}_2$  electroreduction to  $\text{NH}_3$ , *Adv. Energy Mater.*, 2022, **12**, 2103022.
- 62 X. Li, Y. Luo, Q. Li, Y. Guo and K. Chu, Constructing an electron-rich interface over an  $\text{Sb/Nb}_2\text{CT}_x$ -MXene heterojunction for enhanced electrocatalytic nitrogen reduction, *J. Mater. Chem. A*, 2021, **9**, 15955–15962.
- 63 K. Chen, G. Wang, Y. Guo, D. Ma and K. Chu, Iridium single-atom catalyst for highly efficient NO electroreduction to  $\text{NH}_3$ , *Nano Res.*, 2023, DOI: [10.1007/s12274-023-5556-7](https://doi.org/10.1007/s12274-023-5556-7).
- 64 D. Wu, P. Lv, J. Wu, B. He, X. Li, K. Chu, Y. Jia and D. Ma, Catalytic active centers beyond transition metals: atomically dispersed alkaline-earth metals for electroreduction of nitrate to ammonia, *J. Mater. Chem. A*, 2023, **11**, 1817–1828.
- 65 B. He, P. Lv, D. Wu, X. Li, R. Zhu, K. Chu, D. Ma and Y. Jia, Confinement catalysis of a single atomic vacancy assisted by aliovalent ion doping enabled efficient NO electroreduction to  $\text{NH}_3$ , *J. Mater. Chem. A*, 2022, **10**, 18690–18700.
- 66 Y. Wang, A. Xu, Z. Wang, L. Huang, J. Li, F. Li, J. Wicks, M. Luo, D.-H. Nam, C.-S. Tan, Y. Ding, J. Wu, Y. Lum, C.-T. Dinh, D. Sinton, G. Zheng and E. H. Sargent, Enhanced nitrate-to-ammonia activity on copper-nickel alloys via tuning of intermediate adsorption, *J. Am. Chem. Soc.*, 2020, **142**, 5702–5708.